PHYSICAL REVIEW B **109**, 125414 (2024)

Insights into the origin of multiferroicity and large in-plane piezoelectricity in AlXY (X = S, Se; Y = Cl, Br, I) monolayers

Nilakantha Tripathy and Abir De Sarkar[*]
Institute of Nano Science and Technology, Quantum Materials and Devices Unit, Knowledge City, Sector 81, Manauli, Mohali, Punjab 140306, India

(Received 13 November 2023; accepted 21 February 2024; published 14 March 2024)

Understanding the interplay of properties in two-dimensional (2D) multiferroic materials is of paramount importance for crafting the blueprint of cutting-edge functional devices in the next generation. In the present study, we report a family of stable multiferroics AlXY (X = S, Se; Y = Cl, Br, I) with the coexistence of ferroelectricity and ferroelasticity, using density functional theory (DFT) calculations. The AlXY monolayers (MLs) exhibit large in-plane ferroelectric polarization (P_y) ranging from 148 to 177 pC/m with a moderate switching barrier of 0.102–0.192 eV/atom. The polarization in these MLs owes its origin to the repositioning of Al atoms, actuated by soft B_{2u} phonon mode in the paraelectric phase (*Pmmn*). These MLs exhibit robust ferroelasticity with a large reversible strain of 38%–45.1% and moderate switching barriers of 0.175–0.213/eV/atom. The ferroelectric and ferroelastic (FA) phases differ in the electric polarization direction by 90° rotation. Besides a strong anisotropy in mechanical properties, in-plane piezoelectricity and carrier mobilities are observed in the AlXY MLs. Moreover, FA switching provides a highly effective way for finely tuning these anisotropic properties of AlXY MLs. Complementing these findings, we devised an empirical predictive model built on descriptors derived from linear regression analysis, linking atomic polarizability, Bader charge, lattice constant (b), layer thickness (h), bandgap, and effective mass of electron in order to estimate polarization (P_y) and in-plane piezoelectric constants ($d_{22},\ d_{21}$) of AlXY MLs, which is in excellent agreement ($R^2 = 0.95 - 0.98$) with results obtained from DFT.

DOI: 10.1103/PhysRevB.109.125414

I. INTRODUCTION

Multiferroicity, a phenomenon characterized by the simultaneous presence of multiple ferroic properties within a single material, encompasses ferroelectricity, ferroelasticity, and ferromagnetism [1–8]. This intriguing interplay among distinct ferroic states has ushered in innovative avenues for the development of multifunctional devices. Multiferroics have shown particularly interesting phenomena, including the piezoelectric effect [9], giant photovoltaic effect [10], and anisotropic thermoelectric response [11,12]. Ferroelectric (FE) materials exhibit a spontaneous electric polarization that can be reversed by applying an external electric field, making them useful for a wide range of applications, including nonvolatile memories, sensors, actuators, and capacitors [13–16]. For instance, FE random-access memory is a type of nonvolatile memory that uses a FE material as the storage medium, providing high-speed read and write operations, low power consumption, and high endurance [17].

In pursuit of advancements in electronic miniaturization, researchers have invested considerable resources in the quest to thin down FE thin films [18]. However, in ultrathin films, the small thickness induces a large depolarizing field that can suppress the FE dipoles perpendicular to the surface [19–22]. For instance, in ultrathin films of $BaTiO_3$, the polarization exists only when the film thickness is larger than 24 Å, while for $PbTiO_3$ films, the thickness needs to be greater than 12 Å for polarization to occur [21,23]. This phenomenon occurs because the depolarizing field induced by the thin film's small thickness becomes dominant over the FE self-energy, leading to a suppression of the FE polarization [19,20]. To surmount this constraint, researchers have embarked on investigating FE behavior in atomistic monolayers, bilayers, and multilayers, paving the way for the downsizing of FE devices to the atomic scale. Distorted $1T$-MoS_2 [24], $AgBiP_2Se_6$ [25], α-In_2Se_3 [26–28], As_2S_3 [29], group-IV monochalcogenides [4,9,30–33], and SbN [34,35] are some of the FE materials that have been explored. Overall, the exploration of ferroelectricity in atomistic mono- and multilayers holds great promise for developing new materials with enhanced properties and potential applications in a wide range of fields, spanning from electronics to energy storage and conversion [9–12,17].

On a different note, a ferroelastic (FA) substance possesses two or more interchangeable orientations that can be transitioned under external stress, unlocking potential applications in shape memory devices [36]. The FA materials harbor significant promises for utilization in sensing mechanisms and data storage devices, all of which can be modulated through mechanical strains [36–39]. Up until now, various two-dimensional (2D) FA materials have been put forth, encompassing t-YN [37], phosphorene [4], Nb_2SiTe_4 [38], and MPI ($M = \mathrm{Hf},\ \mathrm{Zr}$) [39]. The concurrent presence of ferroelectricity and ferroelasticity in 2D multiferroics presents

---

[*] abir@inst.ac.in, abirdesarkar@gmail.com

a compelling opportunity to adjust electric polarization or shape through either electrical or mechanical means. This holds great potential for crafting multifunctional devices. Also, the interesting part is that the internal strain associated with ferroelasticity is connected to another property called polarization, linked to ferroelectricity. Consequently, the application of an external field aligned with one of these aspects enables the precise manipulation and control of both ferroic orders simultaneously. Therefore, the pursuit of 2D multiferroics with FE-FA coexistence becomes increasingly coveted. Of particular interest are 2D multiferroic materials, which have garnered escalating attention owing to their tremendous potential in the domain of flexible electronics and compact memory devices. Only a handful of potential 2D multiferroics, such as BP_5 [6], group-IV monochalcogenides [4,30], wurtzite monolayers (AB; A = Zn, Cd; B = S, Se, Te) [5], GaTeCl [8], and γ-AlOOH [7] have been put forward, which hinders the progress and potential applications of 2D multiferroics with ferroelectric ferroelasticity. Therefore, it is necessary to investigate for more 2D multiferroics with robust FE-FA coupling.

In the present study, we propose a family of stable 2D multiferroics AlXY (X = S, Se; Y = Cl, Br, I) MLs with in-plane ferroelectricity and ferroelasticity, using first-principles calculations. These MLs exhibit semiconducting behavior with a direct bandgap in the 1.59–3.89 eV range. The AlXY MLs exhibit large in-plane FE polarization (P_y) ranging from 148 to 177 pC/m with a moderate switching barrier of 0.102 to 0.192 eV/atom. Also, these MLs exhibit robust ferroelasticity with a large reversible strain (38%–45.1%) and moderate switching barriers (0.175–0.213 eV/atom). Apart from this, a strong anisotropy in mechanical properties, in-plane piezoelectricity, and carrier mobilities are observed for the AlXY MLs. The atomistic origin of the interplay of the multiferroic properties is unveiled in this work through a systematic investigation. Complementing these findings, we devised an empirical predictive model built on descriptors derived from linear regression analysis to estimate polarization (P_y) and in-plane piezoelectric constants (d_{22}, d_{21}) of AlXY MLs obtained by density functional theory (DFT). These seminal findings are poised to spark exploration in the realm of 2D multiferroics, offering a fertile ground for future investigations and technological innovations. The findings are organized in this paper in a few sections. Moreover, these results are expected to drive future experimental and theoretical research.

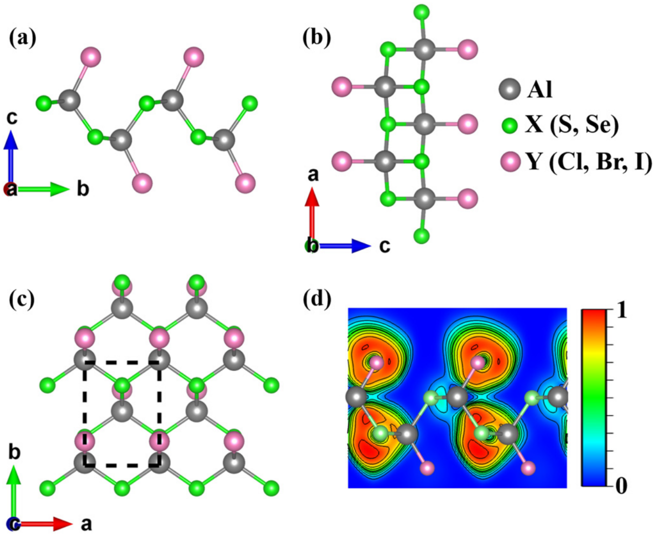

FIG. 1. (a) and (b) are side views, whereas (c) is the top view of AlXY (X = S, Se; Y = Cl, Br, I) MLs. (d) ELF plot of AlSCl ML along the 100 plane.

II. COMPUTATIONAL DETAILS

First-principles calculations based on DFT on materials employed by the Vienna *ab initio* Simulation Package (VASP) [40,41] with the projected-augmented wave method [42]. The Perdew, Burke, and Ernzerhof (PBE) [43] generalized gradient approximation is used to evaluate the exchange-correlation potential. Brillouin zone integration is carried out with a Γ-centered (12 × 8 × 1) Monkhorst-Pack grid [44]. The structures are fully optimized until all the Hellmann-Feynman forces on each atom are less than 0.002 eV/Å, and the total energy difference between two successive steps is smaller than 10^{-7} eV. A vacuum of 15 Å is induced to avoid the periodic integration along the z direction. We have refined our bandgap using the Heyd-Scuseria-Ernzerhof (HSE06) hybrid functional [45] configuring with screening length 0.2 $Å^{-1}$ and setting the mixing rate of the exchange potential to 0.25. The phonon spectra are calculated using the finite displacement method in the PHONOPY program [46]. The supercell of 4 × 4 × 1, which contains 96 atoms with 7 × 5 × 1 k mesh, is taken to calculate the phonon dispersion of AlXY MLs. The *ab initio* molecular dynamics (AIMD) simulation was performed with an *NVT* canonical ensemble using a 3 × 3 × 1 (54 atoms) supercell [47]. The AIMD simulations were performed for 5 ps with 1 fs time step at constant temperature (T = 300 K). The Berry phase method is used to obtain the FE polarization, and the minimum energy pathways for FE and FA transitions are calculated using the climbing image nudged elastic band (Cl-NEB) [48,49].

III. RESULTS AND DISCUSSION

A. Structure and stability

The crystalline structure of bulk AlXY (where X = S, Se; Y = Cl, Br, I) adopts a van der Waals layered structure with an orthorhombic *Pnnm* space group similar to GaTeCl [50]. The thermodynamic stability of bulk AlXY is confirmed by its presence on the convex hull, as characterized by convex hull analysis and extensively elaborated upon in the Supplemental Material (SM) [51]. Figure 1 illustrates the optimized structure of orthorhombic lattice ternary AlXY MLs, characterized by the $Pmn2_1$ (No. 31) space group. These MLs possess a distinctive quadruple-layered configuration, with layers arranged in the sequence Y-(Al-X)-(X-Al)-Y. In this arrangement, the Al atom forms connections with three X (chalcogen) atoms and one Y (halogen) atom. This unique structure lacks an inversion center, thus manifesting FE properties [8,50,57]. Table I presents the optimized lattice parameters (a and b), bond lengths (L), and layer thickness (h). It is observed that both lattice parameters and bond lengths exhibit an increment with the introduction of additional halogen atoms while

TABLE I. The optimized lattice constants (*a* and *b*), bond length (*L*), layer thickness (*h*), exfoliation energy ($E_{\text{exfoliation}}$), cohesive energy (E_{coh}), and bandgap using PBE (E_g^{PBE}) as well as HSE06 (E_g^{HSE06}) functionals for Al*XY* (X = S, Se; Y = Cl, Br, I) MLs. Here "D" stands for direct bandgap.

Al*XY*	a (Å)	b (Å)	$L_{\text{Al}-X}$ (Å)	$L_{\text{Al}-Y}$ (Å)	$L_{\text{Al}-\text{Al}}$ (Å)	h (Å)	$E_{\text{exfoliation}}$ (meV/Å^2)	E_{coh} (eV/atom)	E_g^{PBE} (eV)	E_g^{HSE06} (eV)
AlSCl	3.68	5.34	2.31, 2.30	2.10	3.80	5.57	39	4.04	3.86 (D)	5.11 (D)
AlSBr	3.73	5.36	2.32, 2.31	2.56	3.83	5.94	45	3.81	2.90 (D)	4.00 (D)
AlSI	3.84	5.31	2.34, 2.30	2.48	3.86	6.48	61	3.55	1.59 (D)	2.49 (D)
AlSeCl	3.85	5.58	2.45, 2.44	2.11	3.93	5.52	30	3.75	3.83 (D)	4.92 (D)
AlSeBr	3.88	5.62	2.46, 2.44	2.27	3.96	5.89	29	3.53	3.19 (D)	4.42 (D)
AlSeI	3.97	5.62	2.48, 2.44	2.49	4.01	6.45	38	3.28	2.02 (D)	3.07 (D)

keeping the chalcogen atom constant and vice versa. The calculated exfoliation energies of Al*XY* MLs lie in the range from 29 to 61 meV/Å^2 (as in Table I), which is in the same order of magnitude as experimentally observed in graphene (23 meV/Å^2) by mechanical exfoliation from graphite [58] (see details in the SM). Also, the exfoliation energy of Al*XY* MLs is less than the theoretically predicted MLs such as Ca_2N (68 meV/Å^2) [59], GeP_3 (71 meV/Å^2) [60], and InP_3 (82 meV/Å^2) [61]. The materials possessing energies less than 130 meV/Å^2 are deemed to be potentially exfoliable. Therefore, the exfoliation energy range of Al*XY* MLs suggests the likelihood of their successful exfoliation from the corresponding bulk phase [62]. The chemical bonding within the Al*XY* MLs is further scrutinized using the electron-localized function (ELF), depicted along the (100) plane in Fig. 1(d). The ELF value ranges from 0 (signifying maximum electron delocalization) to 1 (indicative of maximum electron localization), with an ELF of 0.5 representing a free electron cloud. Notably, electrons demonstrate higher localization around *X* and *Y* atoms in comparison to the Al atom. Consequently, bonds between Al-*X* and Al-*Y* exhibit a combination of ionic and covalent characteristics. To delve into the bond strength in Al*XY* MLs, Bader charges (Q_{B}) are computed and tabulated in Table S2 of the Supplemental Material. These charges reveal a transfer of electrons from Al to *X* and *Y* atoms. Furthermore, it is observed that the extent of charge transfer from Al to *X* (*Y*) diminishes with decreasing electronegativity of *X* (*Y*) atoms, leading to a weakened Al-*X* (Al-*Y*) bond in Al*XY* MLs.

To ascertain their dynamical stability, we conducted phonon dispersion spectrum calculations for Al*XY* MLs, illustrated in Fig. 2. These MLs exhibit dynamical stability as they do not feature any imaginary phonon modes in their Brillouin zone. Notably, the phonon frequency range diminishes with an increase in atomic mass of either the *X* (chalcogen) or the *Y* (halogen) atom in Al*XY* MLs. Furthermore, the overlap of low-frequency optical modes with acoustic modes in Al*XY* MLs suggests a propensity for low lattice thermal conductivity [63]. The phonon density of states analysis for Al*XY* MLs indicates that the acoustic and low-frequency optical modes are primarily influenced by the presence of heavier halogen atoms, while the higher-frequency optical modes are predominantly governed by the lighter Al and chalcogen atoms. An intriguing observation arises in the case of AlSCl and AlSeCl MLs. Despite the Se atom having a higher atomic mass compared to the Cl atom, the latter's greater electronegativity, relative to S and Se atoms, significantly influences its contribution to both low- and high-frequency phonon modes in these materials.

The AIMD simulation of Al*XY* MLs at a constant room temperature of 300 K over a 5 ps period is depicted in Fig. S3. Although a slight fluctuation in total energy is observed during the simulation, the final structure of Al*XY* MLs remains intact after 5 ps without conspicuous distortion. This consistency indicates the thermal stability of Al*XY* MLs.

The cohesive energy values listed in Table I serve as a gauge for the MLs' structural integrity. The details of cohesive energy calculation are given in the SM. With cohesive energies ranging from 3.28 to 4.04 eV/atom, Al*XY* MLs demonstrate a level of stability comparable to materials like phosphorene (3.48 eV/atom) [64] and MoS_2 (5.02 eV/atom) [65]. This range suggests promising prospects for their successful synthesis in future experiments.

B. Mechanical properties

We ensured the mechanical stability of Al*XY* MLs by comparing their elastic constants through the strain-energy method [66]. The derived elastic constants, as listed in Table II, meet the Born-Huang criteria [67], $(C_{11}\,C_{22} - C_{12}^2) > 0$, $C_{66} > 0$, affirming the mechanical stability of all Al*XY* MLs. In addition to stability, understanding material strength and anisotropy is crucial for practical applications. To this end, we evaluated angular-dependent elastic properties—Young's modulus $[Y(\theta)]$, Poisson's ratio $[\nu(\theta)]$, and shear modulus $[G(\theta)]$ as shown in Fig. 3, using the following formula [68,69]:

$$Y(\theta) = \frac{\left(C_{11}\,C_{22} - C_{12}^2\right)}{C_{11}\sin^4\theta + C_{22}\cos^4\theta + A\sin^2\theta\cos^2\theta}, \tag{1}$$

$$\nu(\theta) = \frac{C_{12}(\sin^4\theta + \cos^4\theta) - B\sin^2\theta\cos^2\theta}{C_{11}\sin^4\theta + C_{22}\cos^4\theta + A\sin^2\theta\cos^2\theta}, \tag{2}$$

$$G(\theta) = \frac{C_{66}\left(C_{12}^2 - C_{11}C_{22}\right)}{\left(C_{12}^2 - C_{11}C_{22}\right)\left(\cos^2\theta - \sin^2\theta\right)^2 + D\sin^2\theta\cos^2\theta}, \tag{3}$$

where $A = \frac{(C_{11}\,C_{22} - C_{12}^2)}{C_{66}} - 2C_{12}$, $B = C_{11} + C_{22} - \frac{(C_{11}\,C_{22} - C_{12}^2)}{C_{66}}$, and $D = -4C_{66}(C_{11} + C_{22} + 2C_{12})$.

The mechanical properties of Al*XY* MLs, including Young's modulus $[Y(\theta)]$, Poisson's ratio $[\nu(\theta)]$, and shear modulus $[G(\theta)]$, reveal a notable in-plane anisotropy. Table II highlights the maximum (max) and minimum (min) values for

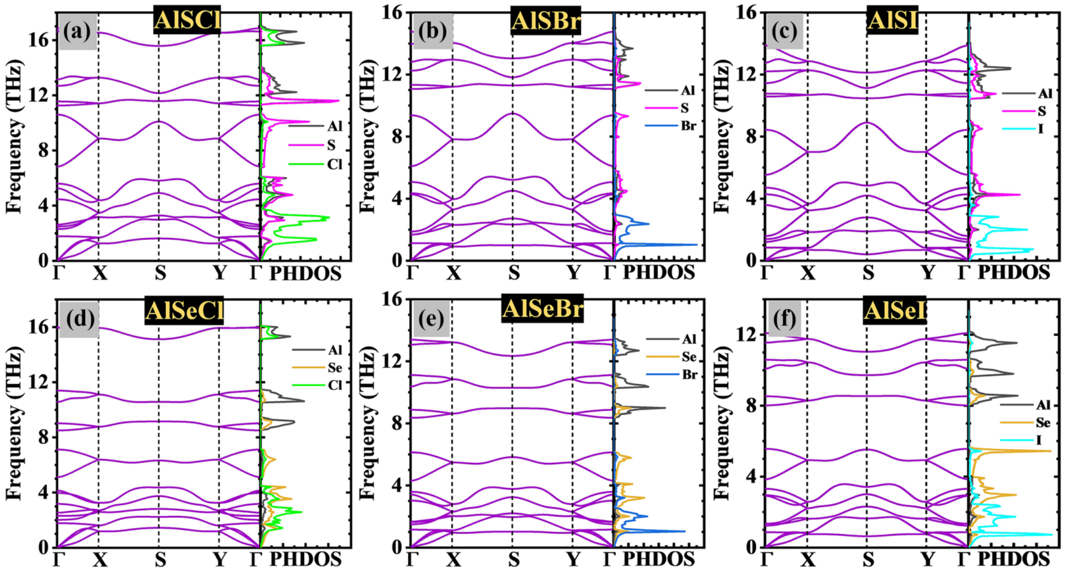

FIG. 2. Phonon dispersion spectra and the corresponding phonon density of states (PHDOS) of AlXY (X = S, Se; Y = Cl, Br, I) MLs.

these properties. Notably, the max (min) Young's modulus is observed along the x (y) direction, while for Poisson's ratio and shear modulus, the max (min) values occur along the x (45° to the x axis) direction. These AlXY MLs demonstrate mechanical flexibility, as evidenced by their low Young's modulus (below ∼66 N/m) compared to Bi_2X_2Y ($X \neq Y$ = S, Se; 60–66 N/m) [70], GaSe (77 N/m) [71], and lower than MoS_2 (124.5 N/m) [72]. This characteristic renders them suitable for applications in flexible electronic devices. With the exception of AlSeCl and AlSeBr, all studied AlXY MLs exhibit a max Poisson's ratio exceeding 0.5, indicative of anisotropic materials [73,74].

To further affirm the mechanical anisotropy of AlXY MLs, universal anisotropy indices (A^{SU}) are presented in Table II, derived through Li's formalism [75–77] (additional details in the SM). A zero A^{SU} denotes a perfectly isotropic elastic response, while deviation from zero indicates varying degrees of anisotropy. The A^{SU} values range between 0.29 and 0.66 for AlXY MLs, underscoring their inherently anisotropic nature. Notably, the ascending order for anisotropic behavior is as follows: AlSeCl < AlSeBr < AlSCl < AlSBr < AlSeI < AlSI.

Examining a material's ultimate strength (σ_U) alongside its elastic properties is vital for assessing its performance under stress. In the case of AlXY MLs, stress-strain curves along orthogonal directions provide valuable insights, as shown in Fig. 4. To account for the 2D structure, stress is normalized by the lattice constant ratio along the z direction (c) to the layer thickness (h), i.e., c/h [78]. Table S3 presents the ultimate stress (σ_U) and corresponding strain (ε_U) for AlXY MLs along both x and y directions. Along the x direction, σ_U ranges from 7.99 to 10.87 GPa, with ε_U spanning in the 18%–24% range. Conversely, along the $y$direction, σ_U ranges from 5.85 to 8.19 GPa, and ε_U ranges from 34% to 36%. Notably, an intriguing trend emerges: as the electronegativity of the chalcogen atom increases while keeping the halogen atom constant in AlXY MLs, σ_U decreases, and ε_U increases along the orthogonal directions. This phenomenon stems from a weakened interaction, as evidenced by the elongation of bond lengths due to the heightened electronegativity of the chalcogen atom. In comparison to materials like MoS_2 and HfS_2 [78], AlXY MLs demonstrate superior flexibility and load-bearing capacity. This is exemplified by their higher ε_U values coupled with significantly lower σ_U values. Such a combination proves advantageous, particularly in applications involving ferroelasticity. These findings highlight the potential of AlXY MLs in scenarios requiring resilience under strain, positioning them as promising candidates for various technological applications, from flexible electronics to advanced materials for structural elements.

TABLE II. Elastic constants (C_{ij}; in N/m), Young's modulus (Y; in N/m), shear modulus (G; in N/m), Poisson's ratio (ν), and universal elastic anisotropy index (A^{SU}) for AlXY MLs are calculated using the relaxed-ion approach.

AlXY	C_{11}	C_{12}	C_{22}	C_{66}	$Y_{\max}$	$Y_{\min}$	$G_{\max}$	$G_{\min}$	$\nu_{\max}$	$\nu_{\min}$	A^{SU}
AlSCl	60.72	9.86	19.99	15.26	55.85	18.39	15.26	11.12	0.49	0.09	0.45
AlSBr	63.55	9.82	19.05	15.24	58.48	17.53	15.24	10.89	0.52	0.07	0.54
AlSI	70.83	9.64	16.48	15.32	65.19	15.17	15.32	10.08	0.58	0.02	0.66
AlSeCl	51.06	9.56	20.22	14.01	46.53	18.43	14.01	10.41	0.47	0.12	0.29
AlSeBr	52.67	9.36	19.07	13.86	48.07	17.41	13.86	10.13	0.49	0.10	0.38
AlSeI	57.35	8.78	16.99	13.76	52.81	15.65	13.76	9.77	0.52	0.07	0.55

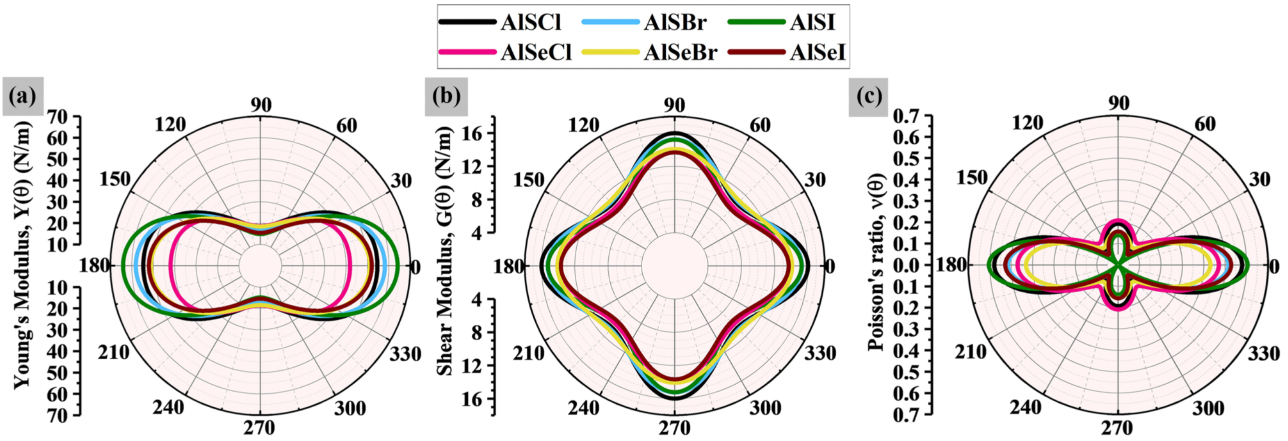

FIG. 3. Angular dependence elastic properties: (a) Young's modulus $Y(\theta)$, (b) shear modulus $G(\theta)$, and (c) Poission's ratio $\nu(\theta)$ of AlXY MLs.

C. Electronic properties

The electrical properties of AlXY MLs were explored by computing their electronic band structure and partial density of states using the PBE functional, as depicted in Fig. 5. The resulting bandgaps are summarized in Table I. A comparison of the band structure using the PBE and hybrid (HSE06) functionals for AlXY MLs is given in Fig. S4. The nature of band dispersion and gaps of AlXY MLs remains unchanged for the HSE06 functional as compared to the PBE functional; only the bandgap widens in the earlier case. Notably, these MLs exhibit a direct bandgap at the Γ point. Additionally, it is observed that the bandgap consistently decreases with increasing halogen atomic numbers for AlSY and AlSeY MLs. The max and min bandgaps are recorded for AlSCl (3.86 eV with PBE and 5.11 eV with HSE06) and AlSI (1.59 eV with PBE and 2.49 eV with HSE06), respectively. Upon closer examination, it is evident that the valence bands primarily consist of p orbitals from X (chalcogen) and Y (halogen) atoms, whereas the conduction bands derive contributions from both s and p orbitals of Al and X atoms.

Further investigation involved applying uniaxial strain along the y direction [$\varepsilon_y = (\frac{b}{b_0} - 1) \times 100\%$] and biaxial strain to the initially unstrained AlXY MLs, aiming to understand their impact on the bandgap. Here, b and b_0 represent the lattice constant along the y direction for the strained and unstrained AlXY MLs, respectively. For AlSY MLs, the bandgap exhibited an increase with uniaxial tensile strain (ε_y). Conversely, for other AlXY MLs under study, the bandgap diminished with increasing tensile ε_y and biaxial strain, as depicted in Fig. S5. Furthermore, as the compressive uniaxial (biaxial) strain increased, the bandgap demonstrated to decrease (increase, up to −3% strain, then a subsequent decrease) for AlXY MLs. However, it is crucial to note that the nature of the bandgap remained unaffected by strain, consistently retaining its direct characteristic for AlXY MLs. Detailed strain-dependent bandgap data and band edge positions are presented in Figs. S5 and S6, offering valuable

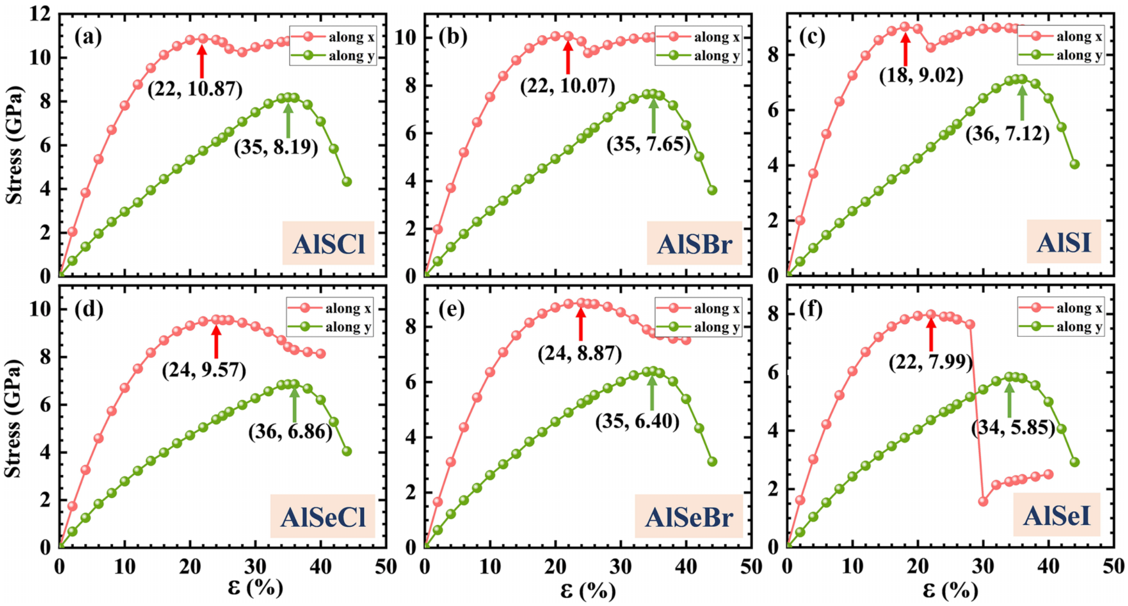

FIG. 4. The stress-strain curve for AlXY MLs under uniaxial tensile strain (ε) along the x and y directions.

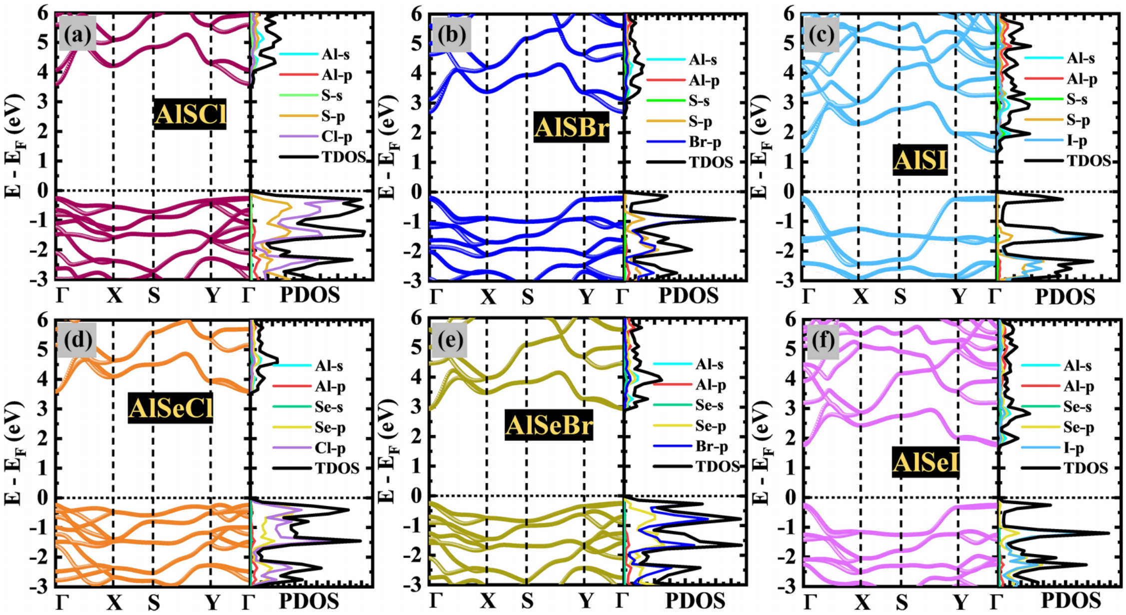

FIG. 5. The calculated electronic band structure and the corresponding partial density of states (PDOS) for Al*XY* MLs using the PBE functional.

insights into how external forces can influence the electronic properties of these promising Al*XY* MLs. These findings open avenues for tailoring their electronic behavior for specific applications in semiconductors and optoelectronic devices.

To delve into the electron transport characteristics of Al*XY* MLs, it is imperative to examine their effective masses and carrier mobilities. Given the anisotropic nature of these MLs, we employ the formalism of Lang *et al.*, rooted in deformation potential (DP) theory, to precisely compute carrier mobilities as follows [79].

$$\mu_{\alpha x} = \frac{e\hbar^3\left(\frac{5C_{11}+3C_{22}}{8}\right)}{k_B T \left(m^*_{\alpha x}\right)^{3/2}\left(m^*_{\alpha y}\right)^{1/2}\left(\frac{9E^2_{\alpha x}+7E_{\alpha x}E_{\alpha y}+4E^2_{\alpha y}}{20}\right)} \times 10^4\ \mathrm{cm}^2\ \mathrm{V}^{-1}\ \mathrm{s}^{-1}, \qquad (4)$$

where the subscript α is the charge carrier (electron or hole) and x or y refers to the propagation direction. $\hbar$, k_B, and T are reduced Planck's constant, Boltzmann constant, and absolute temperature (in this study, $T = 300$ K), respectively. C_{11} and C_{22} are elastic constants along the x and y direction, respectively. m^* and E denote the effective mass and DP, respectively. To quantify the anisotropy in carrier mobility of charge carriers along the x and y directions, we used $R^{\mathrm{ani}}_\alpha = \frac{\max(\mu_{\alpha x},\ \mu_{\alpha y})}{\min(\mu_{\alpha x},\ \mu_{\alpha y})}$ [79].

Table III provides a comprehensive summary of the effective mass and carrier mobilities for Al*XY* MLs (also, see Fig. S7). Notably, the electron mobility along the x direction surpasses that along the y direction by more than 2.5 times, denoted as R^{ani}_α, illustrating a significant anisotropy in electron transport. The highest and lowest electron carrier mobilities along the x direction are observed for AlSI ($237.323\ \mathrm{cm}^2\ \mathrm{V}^{-1}\ \mathrm{s}^{-1}$) and AlSeCl ($110.425\ \mathrm{cm}^2\ \mathrm{V}^{-1}\ \mathrm{s}^{-1}$), respectively. Particularly, these values are on par with the electron mobilities of MoS_2 ($200\ \mathrm{cm}^2\ \mathrm{V}^{-1}\ \mathrm{s}^{-1}$) [80] and InTeI ($156\ \mathrm{cm}^2\ \mathrm{V}^{-1}\ \mathrm{s}^{-1}$) [57]. Remarkably, the electron mobility outperforms the hole mobility by more than sixfold, on account of the low effective electron mass in Al*XY* MLs. With the exception of AlSeCl and AlSeBr, the hole's effective mass along the y direction is strikingly, barely reaching $10\ \mathrm{cm}^2\ \mathrm{V}^{-1}\ \mathrm{s}^{-1}$. This is attributed to the flat valence band along the Γ to Y direction, as elucidated in Fig. 5. Moreover, it is intriguing to note that the carrier mobility of electrons along both x and y directions follows a periodic trend, escalating with the increasing atomic mass of halogen atoms in both AlS*Y* and AlSe*Y* MLs. This behavior underlines the profound impact of atomic composition on the electron transport properties of these materials. To summarize, the incorporation of the DP theory provides a crucial link between the electronic and structural attributes of Al*XY* MLs. This holistic understanding of electron transport behavior is pivotal in assessing the potential and performance of these MLs for electronic applications, propelling advancements in semiconductor technology.

D. Ferroelasticity

Ferroelasticity encompasses phase transition achieved through a structural rearrangement involving a 90° rotation of lattice vectors [4,30]. Within the orthorhombic crystal symmetry of Al*XY* MLs and their $Pmn2_1$ space group, this phenomenon warrants thorough exploration. It involves an initial state where the lattice parameter $a < b$, and a final state where $a' > b'$. Remarkably, both states possess identical ground state energy, wherein $a = b'$ and $b = a'$.This transition, occurring through a paraelastic (PA) state (where $a^* = b^*$), necessitates the calculation of a transition state via the CI-NEB method [49]. A critical factor in initiating FA transition is the external strain tensor described by the Green-Lagrange strain tensor [30,81],

TABLE III. Charge-carrier type (α), DP (E_α; in eV), effective mass (m_α^*; in m_0), elastic constants (C_{11} and C_{22}; in N m^{-1} or J m^{-2}), carrier mobility (μ_α; in $\mathrm{cm}^2\ \mathrm{V}^{-1}\ \mathrm{s}^{-1}$), and anisotropy in carrier mobility (R_α^{ani}) of Al*XY* MLs. Here, m_0 is the mass of the electron, and temperature $T = 300$ K.

Al*XY*	Direction	Carrier type (α)	E_α	m_α^*	C_{11}	C_{22}	M	R_α^{ani}
AlSCl	*x* axis	Electron	9.41	0.22	60.72	19.99	200.55	3.02
	y axis		1.34	1.03			66.34	
	x axis	Hole	4.35	1.10			27.77	6.53
	y axis		0.08	12.30			4.25	
AlSBr	*x* axis	Electron	9.69	0.22	63.55	19.05	205.91	2.94
	y axis		0.91	1.02			70.04	
	x axis	Hole	5.84	0.58			36.54	16.58
	y axis		0.12	16.05			2.20	
AlSI	*x* axis	Electron	9.64	0.22	70.83	16.48	237.32	2.82
	y axis		0.34	1.00			84.02	
	x axis	Hole	8.26	0.33			32.50	59.20
	y axis		0.25	31.04			0.55	
AlSeCl	*x* axis	Electron	9.73	0.28	51.06	20.22	110.42	2.60
	y axis		0.48	1.28			42.45	
	x axis	Hole	2.83	0.75			170.83	2.24
	y axis		1.64	1.75			76.32	
AlSeBr	*x* axis	Electron	9.2	0.26	52.67	19.07	125.86	3.38
	y axis		2.93	1.12			37.28	
	x axis	Hole	4.82	0.75			43.92	5.91
	y axis		0.09	7.80			7.43	
AlSeI	*x* axis	Electron	9.84	0.22	57.35	16.99	169.86	3.32
	y axis		0.24	1.25			51.23	
	x axis	Hole	7.04	0.39			48.08	16.75
	y axis		0.21	10.97			2.87	

$\eta_y = \frac{1}{2}[(H_{\mathrm{PA}}^{-1})^T H_y^T H_y\, H_{\mathrm{PA}}^{-1} - I] = [\varepsilon_{xx}, \varepsilon_{xy};\ \varepsilon_{xy}, \varepsilon_{yy}]$, where I is the 2×2 identity tensor ([1,0;0,1]), H_{PA} is the lattice vector tensor ($[a^*, 0; 0, a^*]$) of the PA state, H_y is the lattice vector tensor ($[a, 0; 0, b]$) FA state, and ε_{xx}, ε_{yy} are tensile or compressive strain along the *x* and *y* directions and ε_{xy} is the shear strain. The pathway of the FA transition for the Al*XY* MLs is visualized in Fig. 6(a). Notably, the PA phase of Al*XY* MLs is dynamically unstable as their phonon spectra exhibit negative frequency at the Γ point (Fig. S8). As a result, the PA phase of Al*XY* MLs can naturally relax in both the *x* and the *y* directions, reaching their respective ground state energy phase (FA phase).

From Table IV, the transformation strain tensor $\eta_y = [-0.145, 0; 0, 0.244]$ for AlSCl ML indicates that 14.5% and 24.4% of compressive and tensile strain are required along the *x* and *y* directions, respectively, to trigger the FA transition. The η_y and the FA energy barrier for Al*XY* MLs are shown in Table IV. The η_y values for Al*XY* MLs notably surpass those of GeSe (2.7% and 4.1%) [4,30] and $\mathrm{Nb_2SiTe_4}$ (−9.8% and 12.1%) [38], underscoring the exceptional FA performance of Al*XY* MLs. The FA energy barrier plays a pivotal role in characterizing ferroelasticity within 2D materials. Al*XY* MLs demonstrate FA energy barriers ranging from 0.175 to 0.213 eV/atom. This energy barrier trend inversely correlates with the electronegativity of the constituent atoms, as observed in Table IV, with AlSCl exhibiting the highest and AlSeI the lowest barrier. Relative to other materials, the energy barriers for FA switching in Al*XY* MLs fall within a moderate range, surpassing GaTeCl (0.16 eV/atom) [8], *M*PI (*M* = Zr, Hf) (0.130–0.141 eV/atom) [39], and lower

TABLE IV. Lattice vector of PA state (a^* Å), the Green-Lagrange strain tensor (η_y), FA reversible strain (R^ε; %), FA barrier energy (E_B^{FA}; eV/atom), FE barrier energy (E_B^{FE}; in eV/atom), spontaneous polarization (P_y; pC/m), piezoelectric stress [e_{22}, e_{21} (pC/m)], and strain [d_{22}, d_{21} (pm/V)] constants for Al*XY* MLs.

Al*XY*	a^*	$\eta_y = [\varepsilon_{xx}, \varepsilon_{xy}; \varepsilon_{yx}, \varepsilon_{yy}]$	R^ε	E_B^{FA}	E_B^{FE}	P_y	e_{22}	e_{21}	d_{22}	d_{21}
AlSCl	4.377	[−0.145,0;0,0.244]	44.7	0.213	0.139	176.48	144.86	−128.52	9.01	−3.58
AlSBr	4.407	[−0.142,0;0,0.239]	43.6	0.206	0.122	167.76	137.02	−149.97	9.14	−3.77
AlSI	4.440	[−0.126,0;0,0.216]	38.2	0.182	0.102	153.12	119.58	−166.02	9.37	−3.62
AlSeCl	4.480	[−0.131,0;0,0.277]	45.1	0.198	0.192	170.63	134.67	−161.76	8.95	−4.84
AlSeBr	4.562	[−0.138,0;0,0.259]	44.8	0.187	0.173	162.62	123.43	−157.67	8.70	−4.54
AlSeI	4.651	[−0.135,0;0,0.229]	41.4	0.175	0.148	148.50	118.28	−172.72	9.24	−4.43

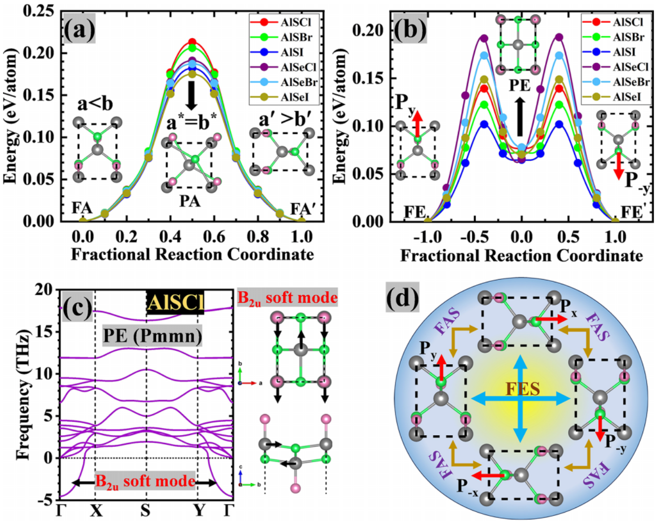

FIG. 6. (a) Ferroelastic (FA) and (b) ferroelectric (FE) transition path calculated using the Cl-NEB method for Al*XY* MLs. (c) Phonon dispersion of the paraelectric (PE) phase for AlSCl ML. (d) Schematic diagram of FA-FE coupling of Al*XY* MLs. The red arrow denotes the direction of polarization.

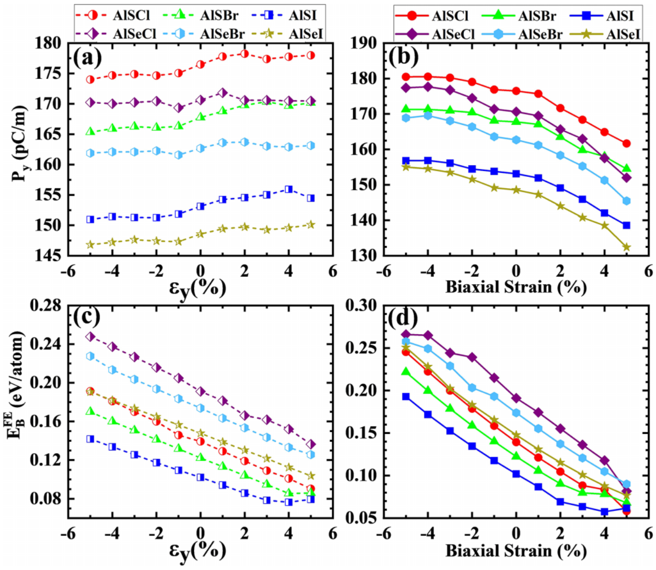

FIG. 7. Variation of polarization (P_y) (a), (b) and FE energy barrier (E_B^{FE}) (c), (d) for Al*XY* MLs under uniaxial (ε_y) and biaxial strain, respectively.

than BP_5 (0.32 eV/atom) [6], but comparable to phosphorene (0.20 eV/atom) [4]. Their moderate FA energy barriers imply robust ferroelasticity even under environmental conditions at room temperature. Apart from the FA energy barrier, FA reversible strain (R^{ε}) ($[\frac{b}{a} - 1] \times 100\%$) is used to characterize the FA performance [38]. The high value of reversible strain leads to a strong FA signal, which is favorable for ferroelectricity. Al*XY* MLs exhibit a reversible strain range of 38%–45.1% (Table IV), indicating a strong FA signal—a favorable characteristic for ferroelectricity. While the reversible strain in Al*XY* MLs is high in comparison to AgF_2 (13.5%) [82], GeS (17.8%) [4], and Nb_2SiTe_4 (24.4%) [38], it is similar to phosphorene (37.9%) [4], BP_5 (41.4%) [6], and GaTeCl (42.4%) [8], albeit lower than stanene (73.2%) [83]. This significant reversible strain solidifies the robustness of FA switching in Al*XY* MLs. The anisotropic mechanical and electronic (effective mass of hole and electron) properties of Al*XY* MLs, influenced by 90° rotation due to FA switching, underscore their potential in controllable electronic devices. This intricate interplay between mechanical and electronic behaviors opens up exciting avenues for the practical application of Al*XY* MLs in advanced technologies.

E. Ferroelectricity

The Al*XY* MLs with $Pmn2_1$ symmetry have mirror reflection to the *yz* plane but no symmetry to the *xz* plane. Consequently, they develop a spontaneous polarization along the *y* direction (P_y). P_y in Al*XY* MLs is determined through the Berry phase method [48], as detailed in Table IV. Notably, among the MLs studied, AlSCl displays the highest P_y value of 176.48 pC/m, oriented along the *y* axis. The P_y value for Al*XY* MLs is in the same range as that of SnSe (187 pC/m) [4] but significantly greater than As_2X_3 (X = S, Se, Te; 18–71 pC/m) [29]. The Al*XY* MLs possess a unique in-plane FE polarization, setting them apart from thin films like perovskite compounds [21,23], which exhibit an out-of-plane polarization. The thickness of the latter is inherently restricted due to the boosted depolarization effect in the out-of-plane direction [19–21]. The energy barrier for the FE phase transition in Al*XY* MLs is presented in Table IV and is calculated using the Cl-NEB method to investigate their robustness. Additionally, Fig. 6(b) illustrates the FE phase transition path through the paraelectric (PE) phase.

In the PE phase, Al*XY* MLs adopt the *Pmmn* space group and possess mirror symmetry along both the *xz* and the *yz* planes. However, these PE structures exhibit dynamic instability due to the presence of a soft optical phonon mode (B_{2u}) located at the Γ point, as depicted in Fig. 6(c) (and Fig. S9). The B_{2u} mode causes displacement of Al atoms along the *y* direction, disrupting the reflection symmetry to the *xz* plane. Consequently, the primary factor responsible for the displacive phase transition from PE (*Pmmn*) to the respective FE ($Pmn2_1$) phase in Al*XY* MLs is this B_{2u} mode. This type of phase transition is also observed in bulk perovskite oxides such as $PbTiO_3$ [84]. The FE energy barrier (E_B^{FE}) of Al*XY* MLs is listed in Table IV. Among Al*XY* MLs, AlSeCl exhibits the highest E_B^{FE} as 0.192 eV/atom, while AlSI has the lowest value as 0.102 eV/atom. These values are comparable to GaTeCl (0.126 eV/atom) [8] and GeS (0.116 eV/atom) [4], but notably lower than SbN (0.227 eV/atom) [35]. The high FE and FA energy barriers arise from the Coulombic repulsion between chalcogen and halogen atoms in Al*XY* MLs.

The remarkable mechanical flexibility of Al*XY* MLs enables them to exhibit altered FE properties when subjected to strain. To scrutinize this effect, both uniaxial (ε_y) and biaxial strains are applied to the initially unstrained Al*XY* MLs. The P_y and E_B^{FE} undergo notable modulation under these applied strains, as shown in Fig. 7. Under uniaxial (ε_y) tensile strain, P_y of Al*XY* MLs initially increases with the gradual rise in strain, reaching a peak before subsequently decreasing. This particular variation in P_y mainly arises from the influence of the electronic dipole moment, as depicted in Fig. S10. However, with the increase in biaxial strain, P_y experiences a reduction of 8%–11% under tensile strain and an increase of 2%–4% under compressive strain, both up to 5% strain for AlXY MLs. In contrast to P_y, E_B^{FE} displays greater responsiveness to strain in AlXY MLs. In the case of uniaxial (ε_y) strain of 5%, E_B^{FE} decreases by 22%–35% under tension and increases by 29%–39% under compression for AlXY MLs. Similarly, at 5% biaxial strain, E_B^{FE} undergoes a substantial reduction of 38%–59% under tension and an increase of 39%–89% under compression relative to the unstrained state. The rapid changes in E_B^{FE} relative to P_y under both uniaxial (ε_y) and biaxial tensile strain signify a promising avenue for their application in memory devices. Overall, for AlXY MLs, the impact of biaxial strain on both P_y and E_B^{FE} is notably more pronounced than uniaxial (ε_y) strain. Furthermore, the trends of P_y and bandgap (E_g) variation with strain are remarkably similar, prompting consideration of bandgap (E_g) as a suitable descriptor for predicting P_y. Overall, these findings highlight the significant influence of mechanical strain on the FE properties of AlXY MLs, opening up avenues for tailored applications in flexible electronics and related fields.

The combination of low Young's modulus and strain tunability ferroelectricity in AlXY MLs provides a compelling incentive to delve into their piezoelectric effect. The piezoelectric stress coefficients (e_{ijk}) are defined as [85]

$$e_{ijk} = \frac{\partial P_i}{\partial \varepsilon_{jk}}. \tag{5}$$

The piezoelectric stress and strain coefficients are related as follows.

$$e_{ijk} = \frac{\partial P_i}{\partial \varepsilon_{jk}} = \frac{\partial P_i}{\partial \sigma_{mn}} \frac{\partial \sigma_{mn}}{\partial \varepsilon_{jk}} = d_{imn} C_{mnjk}, \tag{6}$$

where P_i, ε_{ik}, σ_{mn}, and C_{mnjk} are polarization vector, strain, stress, and elastic tensors, respectively. The subscript $i = 1, 2,$ or 3 in polarization vector P_i are x, y, or z directions, respectively, and jk, $mn = 1$ (xx), 2 (yy), 3 (zz), 4(xz), 5 (yz), or 6 (xy) in strain and stress components as in the Voigt notation. With the $Pmn2_1$ space group, the piezoelectric strain constants of AlXY MLs can be simplified as follows [9].

$$d_{21} = \frac{e_{22}C_{12} - e_{21}C_{22}}{C_{12}^2 - C_{11}C_{22}}, \tag{7}$$

$$d_{22} = \frac{e_{21}C_{12} - e_{22}C_{11}}{C_{12}^2 - C_{11}C_{22}}. \tag{8}$$

The piezoelectric stress coefficient e_{22} (e_{21}) is defined as the change in polarization along the y direction (ΔP_y) with the uniaxial strain ε_y (ε_x). Utilizing the Berry phase approach [48], the relaxed-ion polarization (P_y) is computed under small ε_x or ε_y ranging from -0.01 to 0.01 in increments of 0.005 [3]. The slope of the linear fitting to ΔP_y and ε_x (or ε_y) results in e_{21} (or e_{22}), as shown in Fig. 8. It is worth noting that the piezoelectric coefficients obtained through the relaxed-ion method encompass both electronic and ionic contributions. Thus, for our investigation, we exclusively consider the relaxed-ion method to accurately capture the piezoelectric behavior. The obtained e_{22} coefficient is $+ve$, while e_{21} is $-ve$ for AlXY MLs. The $-ve$ e_{21} coefficient indicates that the P_y value diminishes with increasing uniaxial tensile strain along the x direction (ε_x), as illustrated in Fig. 8(a). Table IV provides the computed in-plane piezoelectric stress (e_{22}, e_{21}) and strain (d_{22}, d_{21}) coefficients for AlXY MLs. Intriguingly, the e_{22} (e_{21}) coefficient tends to decrease (increase) with increasing halogen atomic number, while the d_{22} (d_{21}) coefficient displays an opposite trend. The highest (lowest) e_{22} value is 144.86 (118.28) pC/m for AlSCl (AlSeI) ML. Similarly, the highest (lowest) e_{21} value is -172.72 (-128.52) pC/m for AlSeI (AlSCl) ML. When it comes to the strain coefficients (d_{22} and d_{21}), AlSI ML demonstrates the maximum response with a value of 9.37 pm/V for d_{22} and -4.54 pm/V for d_{21}. Conversely, AlSeCl ML exhibits the minimum response, with d_{22} and d_{21} values of 8.70 and -3.58 pm/V, respectively. The in-plane piezoelectric strain constants of AlXY MLs are large comparing to α-XN (X = P, As, Sb; $d_{11} = 1.63$ to 7.69 pm/V, $d_{12} = -2.65$ to -5.93 pm/V) [86], MoS$_2$ ($d_{11} = 3.7$ pm/V) [85], and GaSe ($d_{11} = 2.3$ pm/V) [87]. Remarkably, AlSY (AlSeY) MLs exhibit a more robust piezoelectric response under uniaxial strain along the y (x) direction, owing to their elevated d_{22} (d_{21}) values in comparison to AlSeY (AlSY) MLs. In summary, the investigation reveals intriguing trends in the piezoelectric properties of AlXY MLs, shedding light on their potential applications in piezoelectric devices and flexible electronics.

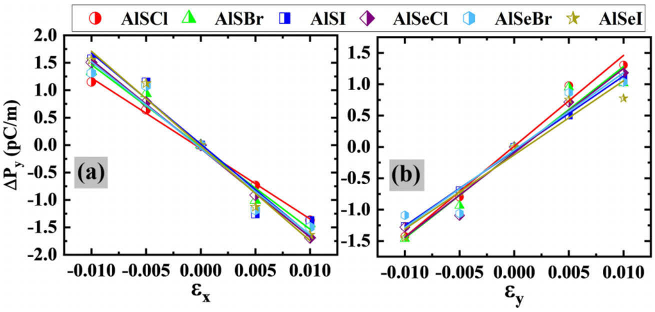

FIG. 8. The change in relaxed-ion polarization along y (ΔP_y) with uniaxial strain (a) along x (ε_x) and (b) along y (ε_x) for AlXY MLs. The in-plane piezoelectric coefficients e_{21} and e_{22} are calculated from the slope of plots (a) and (b), respectively.

Recently, Blonsky *et al.* proposed an empirical formula to elucidate the periodic trend of piezoelectric constants in binary 2D MLs [85]. However, this model falls short when applied to multicomponent systems. In light of this, our current study takes into account a range of primary descriptors, each serving a distinct purpose. These include structural parameters like lattice parameter (b) and thickness (h), Bader charges (Q_{B}) as charge descriptor, atomic polarizability (α) as a dipole moment descriptor, alongside charge-carrier descriptors such as bandgap (E_g), and effective mass of the electron ($M_e^* = \sqrt{m_{ex}^* m_{ey}^*}$). These descriptors collectively form the basis for unraveling the polarization (P_y) and in-plane piezoelectric strain constants (d_{22}, d_{21}) of AlXY MLs. The atomic polarizabilities (α) of Al, S, Se, Cl, Br, and I, derived from the work of Schwerdtfeger and Nagle, are as follows: 57.8, 19.4, 29, 16.6, 21, and 32.9 a.u., respectively [88]. These values serve as crucial inputs in our analysis. To scrutinize the relationship between these descriptors and the polarization and piezoelectric constants, we employ the Pearson correlation method, as

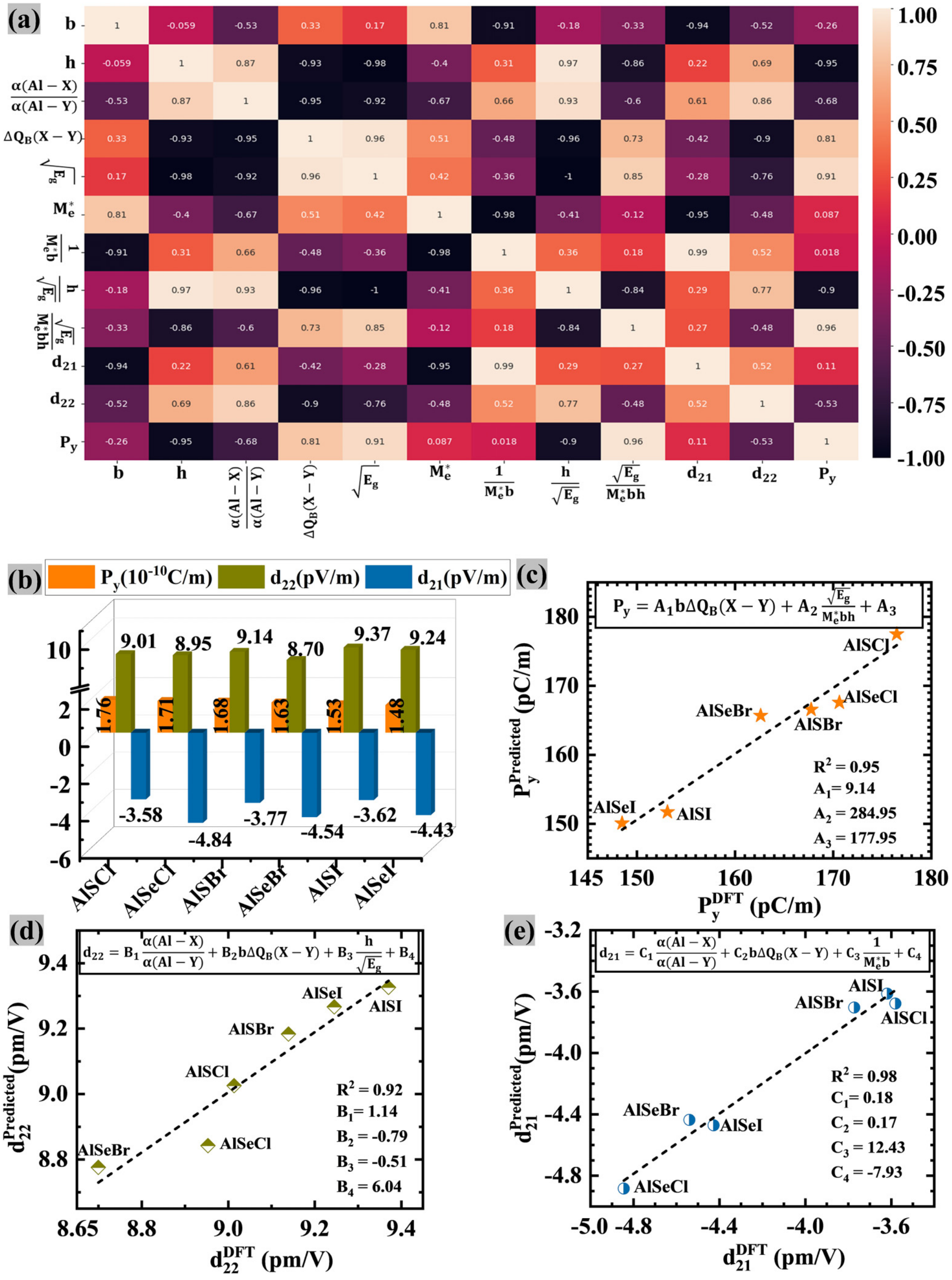

	b	h	$\frac{\alpha(\mathrm{Al}-X)}{\alpha(\mathrm{Al}-Y)}$	$\Delta Q_B(X-Y)$	$\sqrt{E_g}$	M_e^*	$\frac{1}{M_e^* b}$	$\frac{h}{\sqrt{E_g}}$	$\frac{\sqrt{E_g}}{M_e^* bh}$	d_{21}	d_{22}	P_y
b	1	-0.059	-0.53	0.33	0.17	0.81	-0.91	-0.18	-0.33	-0.94	-0.52	-0.26
h	-0.059	1	0.87	-0.93	-0.98	-0.4	0.31	0.97	-0.86	0.22	0.69	-0.95
$\frac{\alpha(\mathrm{Al}-X)}{\alpha(\mathrm{Al}-Y)}$	-0.53	0.87	1	-0.95	-0.92	-0.67	0.66	0.93	-0.6	0.61	0.86	-0.68
$\Delta Q_B(X-Y)$	0.33	-0.93	-0.95	1	0.96	0.51	-0.48	-0.96	0.73	-0.42	-0.9	0.81
$\sqrt{E_g}$	0.17	-0.98	-0.92	0.96	1	0.42	-0.36	-1	0.85	-0.28	-0.76	0.91
M_e^*	0.81	-0.4	-0.67	0.51	0.42	1	-0.98	-0.41	-0.12	-0.95	-0.48	0.087
$\frac{1}{M_e^* b}$	-0.91	0.31	0.66	-0.48	-0.36	-0.98	1	0.36	0.18	0.99	0.52	0.018
$\frac{h}{\sqrt{E_g}}$	-0.18	0.97	0.93	-0.96	-1	-0.41	0.36	1	-0.84	0.29	0.77	-0.9
$\frac{\sqrt{E_g}}{M_e^* bh}$	-0.33	-0.86	-0.6	0.73	0.85	-0.12	0.18	-0.84	1	0.27	-0.48	0.96
d_{21}	-0.94	0.22	0.61	-0.42	-0.28	-0.95	0.99	0.29	0.27	1	0.52	0.11
d_{22}	-0.52	0.69	0.86	-0.9	-0.76	-0.48	0.52	0.77	-0.48	0.52	1	-0.53
P_y	-0.26	-0.95	-0.68	0.81	0.91	0.087	0.018	-0.9	0.96	0.11	-0.53	1

FIG. 9. For AlXY MLs, (a) Pearson correlation analysis of the polarization (P_y) and the in-plane piezoelectric strain constants (d_{22}, d_{21}) with different descriptors, (b) histogram plot of P_y, d_{22}, and d_{21} obtained from DFT calculation, and comparison of predicted (c) P_y, (d) d_{22}, and (e) d_{21} obtained by our model with their respective DFT results.

illustrated in Fig. 9(a). Through this approach, we identify the descriptors that exhibit the highest correlation coefficients with the polarization and piezoelectric constants. Taking into account these maximum correlation coefficients, our primary model evolves as follows:

$$P_y, d_{22}, d_{21} \propto b\Delta Q_{\mathrm{B}}(X-Y), \tag{9}$$

$$d_{22}, d_{21} \propto \frac{\alpha(\mathrm{Al}-X)}{\alpha(\mathrm{Al}-Y)}, \tag{10}$$

$$d_{22} \propto \frac{h}{\sqrt{E_g}}, \tag{11}$$

$$d_{21} \propto \frac{1}{M_e^* b}, \tag{12}$$

$$P_y \propto \frac{\sqrt{E_g}}{M_e^* bh}. \tag{13}$$

The final model for predicting the polarization (P_y) and piezoelectric constants (d_{22} and d_{21}) is established through a linear combination of the aforementioned primary and secondary descriptors specific to the AlXY MLs, where

$$P_y = A_1 b \Delta Q_{\mathrm{B}}(X - Y) + A_2 \frac{\sqrt{E_g}}{M_e^* b h} + A_3, \qquad (14)$$

$$d_{22} = B_1 \frac{\alpha(\mathrm{Al} - X)}{\alpha(\mathrm{Al} - Y)} + B_2 b \Delta Q_{\mathrm{B}}(X - Y) + B_3 \frac{h}{\sqrt{E_g}} + B_4, \qquad (15)$$

$$d_{21} = C_1 \frac{\alpha(\mathrm{Al} - X)}{\alpha(\mathrm{Al} - Y)} + C_2 b \Delta Q_{\mathrm{B}}(X - Y) + C_3 \frac{1}{M_e^* b} + C_4. \qquad (16)$$

The fitting coefficients, crucial for our model's accuracy, are outlined in Table S4. A high R-squared (R^2) value, approaching 1, signifies the model's reliability in comparison to DFT results. In our current study, we achieve R^2 values of 0.95, 0.92, and 0.98 for our P_y, d_{22}, and d_{21} models [Eqs. (14), (15), and (16), respectively], in agreement with DFT results. These high R^2 values affirm the robustness and accuracy of the proposed models, as visualized in Figs. 9(c)–9(e). We discern that, in addition to the Bader charge difference [$\Delta Q_{\mathrm{B}}(X - Y)$], polarization is directly influenced by the square root of the bandgap ($\sqrt{E_g}$). This observation suggests that widening the bandgap has the potential to enhance the polarization of AlXY MLs. Moreover, our model indicates that, apart from the Bader charge difference [$\Delta Q_{\mathrm{B}}(X - Y)$] and the ratio of atomic polarizability ($\frac{\alpha(\mathrm{Al}-X)}{\alpha(\mathrm{Al}-Y)}$), the piezoelectric constants of AlXY MLs also hinge inversely either on the square root of the bandgap ($\sqrt{E_g}$) or on the effective mass of the electron (M_e^*), providing valuable insights for further material design and engineering considerations.

IV. CONCLUSION

In summary, we conducted a comprehensive first-principles study to analyze the ferroelasticity, ferroelectricity, and strong in-plane piezoelectric behavior in AlXY ($X =$ S and Se; $Y =$ Cl, Br, and I) MLs. These MLs demonstrate significant mechanical anisotropy, as evidenced by the universal anisotropy index (A^{SU}) and the angle-dependent measurements of Young's modulus, Poisson's ratio, and shear modulus. Notably, the low elastic constants and Young's modulus (less than 66 N/m) render the AlXY MLs flexible. These MLs are multiferroics and possess a direct bandgap within the range of 1.59–3.89 eV (2.49–5.11 eV) with the PBE (HSE06) functional. The AlXY MLs exhibit robust ferroelasticity with a large reversible strain (38%–45.1%) and moderate FA energy barriers (0.175–0.213 eV/atom). Additionally, these MLs feature in-plane ferroelectricity with moderate P_y (148–176 pC/m) and E_B^{FE} (0.102–0.192 eV/atom). This in-plane polarization effectively mitigates depolarization effects stemming from the perovskitelike FE thin-film thickness. Also, the primary factor responsible for the displacive phase transition from the PE (*Pmmn*) to the respective FE ($Pmn2_1$) phase in AlXY MLs is the soft B_{2u} mode. The interchange between the FE phase and the FA phase allows a 90° rotation in the electric polarization direction. For AlXY MLs, the impact of biaxial strain on both P_y and E_B^{FE} is notably more pronounced than uniaxial (ε_y) strain. With the increase in biaxial strain, P_y (E_B^{FE}) experiences a reduction of 8%–11% (38%–59%) under tensile strain and an increase of 2%–4% (39%–89%) under compressive strain, both up to 5% strain for AlXY MLs, which is useful for memory devices. Apart from this, these MLs demonstrate strong anisotropic in-plane piezoelectric strain coefficients, where d_{22} spans from 8.70 to 9.37 pm/V and d_{21} ranges from −3.58 to −4.54 pm/V. To sum up, by leveraging a statistical analysis, we have formulated the empirical models for polarization and piezoelectric constants based on the modern theory of polarization. These models show excellent agreement ($R^2 = 0.95 - 0.98$) with DFT results and are specifically tailored to encompass the entire AlXY MLs, operating at the intricate atomic level. Therefore, these compelling characteristics collectively position AlXY MLs as promising candidates for 2D multiferroics and hold great potential in advancing next-generation technology across a diverse spectrum of applications.

ACKNOWLEDGMENTS

N.T. acknowledges the financial support provided by the Council of Scientific and Industrial Research (CSIR), India (Grant No. 09/1129(0029)/2020-EMR-I). The calculations were performed using the in-house computational facility of the Institute of Nano Science and Technology (INST). We are also grateful to the PARAM-Smriti Facility at the National Agri-Food Biotechnology Institute (NABI), under the National Supercomputing Mission, Government of India, for providing computational resources.

---

[1] M. Wu, Two-dimensional van der Waals ferroelectrics: Scientific and technological opportunities, ACS Nano **15**, 9229 (2021).

[2] D. Li, P. Liu, R. He, Y. Bai, C. Liu, B. Wang, and G. Jia, Intrinsic multiferroicity and magnetoelectric coupling in VSI$_2$ monolayer, Appl. Phys. Lett. **123**, 052902 (2023).

[3] C. Zhang, Y. Nie, S. Sanvito, and A. Du, First-principles prediction of a room-temperature ferromagnetic Janus VSSe monolayer with piezoelectricity, ferroelasticity, and large valley polarization, Nano Lett. **19**, 1366 (2019).

[4] M. Wu and X. C. Zeng, Intrinsic ferroelasticity and/or multiferroicity in two-dimensional phosphorene and phosphorene analogues, Nano Lett. **16**, 3236 (2016).

[5] Z. Ma, P. Huang, J. Li, P. Zhang, J. Zheng, W. Xiong, F. Wang, and X. Zhang, Multiferroicity and giant in-plane negative Poisson's ratio in wurtzite monolayers, npj Comput. Mater. **8**, 51 (2022).

[6] H. Wang, X. Li, J. Sun, Z. Liu, and J. Yang, BP$_5$ monolayer with multiferroicity and negative Poisson's ratio: A prediction by global optimization method, 2D Mater. **4**, 045020 (2017).

[7] C. Liu, R. Gao, X. Cheng, X. Yang, G. Qin, H. Gao, S. Picozzi, and W. Ren, First-principles study of ferroelectricity, antiferroelectricity, and ferroelasticity in two-dimensional γ-AlOOH, Phys. Rev. B **107**, L121402 (2023).

[8] S.-H. Zhang and B.-G. Liu, A controllable robust multiferroic GaTeCl monolayer with colossal 2D rerroelectricity

and desirable multifunctionality, Nanoscale **10**, 5990 (2018).

[9] R. Fei, W. Li, J. Li, and L. Yang, Giant piezoelectricity of monolayer group IV monochalcogenides: SnSe, SnS, GeSe, and GeS, Appl. Phys. Lett. **107**, 173104 (2015).

[10] T. Rangel, B. M. Fregoso, B. S. Mendoza, T. Morimoto, J. E. Moore, and J. B. Neaton, Large bulk photovoltaic effect and spontaneous polarization of single-layer monochalcogenides, Phys. Rev. Lett. **119**, 067402 (2017).

[11] D. Sarkar, T. Ghosh, S. Roychowdhury, R. Arora, S. Sajan, G. Sheet, U. V. Waghmare, and K. Biswas, Ferroelectric instability induced ultralow thermal conductivity and high thermoelectric performance in rhombohedral *p*-type GeSe crystal, J. Am. Chem. Soc. **142**, 12237 (2020).

[12] L. Medrano Sandonas, D. Teich, R. Gutierrez, T. Lorenz, A. Pecchia, G. Seifert, and G. Cuniberti, Anisotropic thermoelectric response in two-dimensional puckered structures, J. Phys. Chem. C **120**, 18841 (2016).

[13] X. Wei, N. Domingo, Y. Sun, N. Balke, R. E. Dunin-Borkowski, and J. Mayer, Progress on emerging ferroelectric materials for energy harvesting, storage and conversion, Adv. Energy Mater. **12**, 2201199 (2022).

[14] H. Huang and J. F. Scott, *Ferroelectric Materials for Energy Applications* (Wiley, New York, 2018), p. 265.

[15] T. Y. Kim, S. K. Kim, and S.-W. Kim, Application of ferroelectric materials for improving output power of energy harvesters, Nano Convergence **5**, 30 (2018).

[16] J. F. Scott and C. A. Paz de Araujo, Ferroelectric memories, Science **246**, 1400 (1989).

[17] Y. Joo, E. Hwang, H. Hong, S. Cho, and H. Yang, Memory and synaptic devices based on emerging 2D ferroelectricity, Adv. Electron. Mater. **9**, 2300211 (2023).

[18] N. Setter, D. Damjanovic, L. Eng, G. Fox, S. Gevorgian, S. Hong, A. Kingon, H. Kohlstedt, N. Y. Park, G. B. Stephenson, and I. Stolitchnov, Ferroelectric thin films: Review of materials, properties, and applications, J. Appl. Phys. **100**, 051606 (2006).

[19] P. Wurfel, I. P. Batra, and J. T. Jacobs, Polarization instability in thin ferroelectric films, Phys. Rev. Lett. **30**, 1218 (1973).

[20] R. R. Mehta, B. D. Silverman, and J. T. Jacobs, Depolarization fields in thin ferroelectric films, J. Appl. Phys. **44**, 3379 (1973).

[21] J. Junquera and P. Ghosez, Critical thickness for ferroelectricity in perovskite ultrathin films, Nature (London) **422**, 506 (2003).

[22] C. H. Ahn, K. M. Rabe, and J.-M. Triscone, Ferroelectricity at the nanoscale: Local polarization in oxide thin films and heterostructures, Science **303**, 488 (2004).

[23] D. D. Fong, G. B. Stephenson, S. K. Streiffer, J. A. Eastman, O. Auciello, P. H. Fuoss, and C. Thompson, Ferroelectricity in ultrathin perovskite films, Science **304**, 1650 (2004).

[24] A. Lipatov, P. Chaudhary, Z. Guan, H. Lu, G. Li, O. Crégut, K. D. Dorkenoo, R. Proksch, S. Cherifi-Hertel, D. F. Shao, and E. Y. Tsymbal, Direct observation of ferroelectricity in two-dimensional MoS_2, npj 2D Mater. Appl. **6**, 18 (2022).

[25] B. Xu, H. Xiang, Y. Xia, K. Jiang, X. Wan, J. He, J. Yin, and Z. Liu, Monolayer $AgBiP_2Se_6$: An atomically thin ferroelectric semiconductor with out-plane polarization, Nanoscale **9**, 8427 (2017).

[26] M. Soleimani and M. Pourfath, Ferroelectricity and phase transitions in In_2Se_3 van der Waals material, Nanoscale **12**, 22688 (2020).

[27] Y. Zhou, D. Wu, Y. Zhu, Y. Cho, Q. He, X. Yang, K. Herrera, Z. Chu, Y. Han, M. C. Downer, and H. Peng, Out-of-plane piezoelectricity and ferroelectricity in layered α-In_2Se_3 nanoflakes, Nano Lett. **17**, 5508 (2017).

[28] W. Ding, J. Zhu, Z. Wang, Y. Gao, D. Xiao, Y. Gu, Z. Zhang, and W. Zhu, Prediction of intrinsic two-dimensional ferroelectrics in In_2Se_3 and other III_2-VI_3 van der Waals materials, Nat. Commun. **8**, 14956 (2017).

[29] W. Gao and J. R. Chelikowsky, Prediction of intrinsic ferroelectricity and large piezoelectricity in monolayer arsenic chalcogenides, Nano Lett. **20**, 8346 (2020).

[30] H. Wang and X. Qian, Two-dimensional multiferroics in monolayer group IV monochalcogenides, 2D Mater. **4**, 015042 (2017).

[31] S. Barraza-Lopez, T. P. Kaloni, S. P. Poudel, and P. Kumar, Tuning the ferroelectric-to-paraelectric transition temperature and dipole orientation of group-IV monochalcogenide monolayers, Phys. Rev. B **97**, 024110 (2018).

[32] M. Mehboudi, B. M. Fregoso, Y. Yang, W. Zhu, A. van der Zande, J. Ferrer, L. Bellaiche, P. Kumar, and S. Barraza-Lopez, Structural phase transition and material properties of few-layer monochalcogenides, Phys. Rev. Lett. **117**, 246802 (2016).

[33] R. Fei, W. Kang, and L. Yang, Ferroelectricity and phase transitions in monolayer group-IV monochalcogenides, Phys. Rev. Lett. **117**, 097601 (2016).

[34] Y. Zhang, T. Ouyang, C. He, J. Li, and C. Tang, Extremely promising monolayer materials with robust ferroelectricity and extraordinary piezoelectricity: Δ-AsN, δ-SbN, and δ-BiN, Nanoscale **15**, 6363 (2023).

[35] C. Liu, W. Wan, J. Ma, W. Guo, and Y. Yao, Robust ferroelectricity in two-dimensional SbN and BiP, Nanoscale **10**, 7984 (2018).

[36] E. K. H. Salje, Ferroelastic materials, Annu. Rev. Mater. Res. **42**, 265 (2012).

[37] B. Xu, H. Xiang, J. Yin, Y. Xia, and Z. Liu, A two-dimensional tetragonal yttrium nitride monolayer: A ferroelastic semiconductor with switchable anisotropic properties, Nanoscale **10**, 215 (2018).

[38] T. Zhang, Y. Ma, X. Xu, C. Lei, B. Huang, and Y. Dai, Two-dimensional ferroelastic semiconductors in Nb_2SiTe_4 and Nb_2GeTe_4 with promising electronic properties, J. Phys. Chem. Lett. **11**, 497 (2020).

[39] T. Zhang, Y. Ma, L. Yu, B. Huang, and Y. Dai, Direction-control of anisotropic electronic behaviors via ferroelasticity in two-dimensional α-MPI (M = Zr, Hf), Mater. Horiz. **6**, 1930 (2019).

[40] G. Kresse and J. Furthmüller, Efficiency of ab-initio total energy calculations for metals and semiconductors using a plane-wave basis set, Comput. Mater. Sci. **6**, 15 (1996).

[41] G. Kresse and J. Furthmüller, Efficient iterative schemes for *ab initio* total-energy calculations using a plane-wave basis set, Phys. Rev. B **54**, 11169 (1996).

[42] P. E. Blöchl, Projector augmented-wave method, Phys. Rev. B **50**, 17953 (1994).

[43] J. P. Perdew, K. Burke, and M. Ernzerhof, Generalized gradient approximation made simple, Phys. Rev. Lett. **77**, 3865 (1996).

[44] H. J. Monkhorst and J. D. Pack, Special points for Brillouin-zone integrations, Phys. Rev. B **13**, 5188 (1976).

[45] J. Heyd, G. E. Scuseria, and M. Ernzerhof, Hybrid functionals based on a screened Coulomb potential, J. Chem. Phys. **118**, 8207 (2003).

[46] A. Togo and I. Tanaka, First principles phonon calculations in materials science, Scr. Mater. **108**, 1 (2015).

[47] R. N. Barnett and U. Landman, Born-Oppenheimer molecular-dynamics simulations of finite systems: Structure and dynamics of $(H_2O)_2$, Phys. Rev. B **48**, 2081 (1993).

[48] R. D. King-Smith and D. Vanderbilt, Theory of polarization of crystalline solids, Phys. Rev. B **47**, 1651 (1993).

[49] G. Henkelman, B. P. Uberuaga, and H. Jónsson, A climbing image nudged elastic band method for finding saddle points and minimum energy paths, J. Chem. Phys. **113**, 9901 (2000).

[50] R. Kniep, A. Wilms, and H. J. Beister, Phase relations in Ga_2X_3-GaY_3 systems ($X = $ Se,Te; $Y = $ Cl,Br,I)—Crystal growth, structural relations and optical absorption of intermediate compounds GaXY, Mater. Res. Bull. **18**, 615 (1983).

[51] See Supplemental Material at http://link.aps.org/supplemental/10.1103/PhysRevB.109.125414 for more details on convex hull, exfoliation energy, Bader charges, cohesive energy, AIMD simulation, ultimate stress and strain, effect of strain on bandgap and band edge, phonon spectra of paraelastic and paraelectric phase, electronic and ionic dipole moment with strain and the fitting coefficients to the empirical model for polarization and piezoelectric strain coefficients of AlXY ($X = $ S, Se; $Y = $ Cl, Br, I) monolayers. It also contains Refs. [52–56].

[52] J. E. Saal, S. Kirklin, M. Aykol, B. Meredig, and C. Wolverton, Materials design and discovery with high-throughput density functional theory: The Open Quantum Materials Database (OQMD), JOM **65**, 1501 (2013).

[53] S. P. Ong, W. D. Richards, A. Jain, G. Hautier, M. Kocher, S. Cholia, D. Gunter, V. L. Chevrier, K. A. Persson, and G. Ceder, Python materials genomics (pymatgen): A robust, open-Source Python library for materials analysis, Comput. Mater. Sci. **68**, 314 (2013).

[54] R. Wang, W. Xia, T. J. Slade, X. Fan, H. Dong, K.-M. Ho, P. C. Canfield, and C.-Z. Wang, Machine learning guided discovery of ternary compounds involving La and immiscible Co and Pb elements, npj Comput. Mater. **8**, 258 (2022).

[55] C. J. Bartel, A. Trewartha, Q. Wang, A. Dunn, A. Jain, and G. Ceder, A critical examination of compound stability predictions from machine-learned formation energies, npj Comput. Mater. **6**, 97 (2020).

[56] J. H. Jung, C.-H. Park, and J. Ihm, A rigorous method of calculating exfoliation energies from first principles, Nano Lett. **18**, 2759 (2018).

[57] A. Kishore, N. Tripathy, and A. De Sarkar, Unconventional anisotropy in excitonic properties and carrier mobility in iodine-based XTeI (X = Ga, In) monolayers for visible-light photocatalytic water splitting, J. Phys. Chem. C **127**, 1992 (2023).

[58] W. Wang, S. Dai, X. Li, J. Yang, D. J. Srolovitz, and Q. Zheng, Measurement of the cleavage energy of graphite, Nat. Commun. **6**, 7853 (2015).

[59] S. Zhao, Z. Li, and J. Yang, Obtaining two-dimensional electron gas in free space without resorting to electron doping: An electride based design, J. Am. Chem. Soc. **136**, 13313 (2014).

[60] Y. Jing, Y. Ma, Y. Li, and T. Heine, GeP_3: A small indirect band gap 2D crystal with high carrier mobility and strong interlayer quantum confinement, Nano Lett. **17**, 1833 (2017).

[61] N. Miao, B. Xu, N. C. Bristowe, J. Zhou, and Z. Sun, Tunable magnetism and extraordinary sunlight absorbance in indium triphosphide monolayer, J. Am. Chem. Soc. **139**, 11125 (2017).

[62] C. M. O. Bastos, R. Besse, J. L. F. Da Silva, and G. M. Sipahi *ab initio* investigation of structural stability and exfoliation energies in transition metal dichalcogenides based on Ti-, V-, and Mo-group elements, Phys. Rev. Mater. **3**, 044002 (2019).

[63] N. Wang, M. Li, H. Xiao, X. Zu, and L. Qiao, Layered LaCuOSe: A promising anisotropic thermoelectric material, Phys. Rev. Appl. **13**, 024038 (2020).

[64] J. Guan, Z. Zhu, and D. Tománek, Phase coexistence and metal-insulator transition in few-layer phosphorene: A computational study, Phys. Rev. Lett. **113**, 046804 (2014).

[65] Y. Ding, Y. Wang, J. Ni, L. Shi, S. Shi, and W. Tang, First principles study of structural, vibrational and electronic properties of graphene-like MX_2 (M = Mo, Nb, W, Ta; X = S, Se, Te) monolayers, Phys. B (Amsterdm, Neth.) **406**, 2254 (2011).

[66] M. J. Varjovi, M. E. Kilic, and E. Durgun, Ternary pentagonal BNSi monolayer: Two-dimensional structure with potentially high carrier mobility and strong excitonic effects for photocatalytic applications, Phys. Rev. Mater. **6**, 034004 (2022).

[67] F. Mouhat and F.-X. Coudert, Necessary and sufficient elastic stability conditions in various crystal systems, Phys. Rev. B **90**, 224104 (2014).

[68] X. Liu, Z. Zhang, Z. Ding, B. Lv, Z. Luo, J.-S. Wang, and Z. Gao, Highly anisotropic electronic and mechanical properties of monolayer and bilayer As_2S_3, Appl. Surf. Sci. **542**, 148665 (2021).

[69] Cz. Jasiukiewicz, T. Paszkiewicz, and S. Wolski, Auxetic properties and anisotropy of elastic material constants of 2D crystalline media, Phys. Status Solidi B **245**, 562 (2008); **247**, 1247 (2010).

[70] N. Tripathy and A. De Sarkar, Anisotropy in colossal piezoelectricity, giant Rashba effect and ultrahigh carrier mobility in Janus structures of quintuple Bi_2X_3 (X = S, Se) monolayers, J. Phys.: Condens. Matter **35**, 335301 (2023).

[71] M. Yagmurcukardes, R. T. Senger, F. M. Peeters, and H. Sahin, Mechanical properties of monolayer GaS and GaSe crystals, Phys. Rev. B **94**, 245407 (2016).

[72] D. Çakır, F. M. Peeters, and C. Sevik, Mechanical and thermal properties of h-MX_2 (M = Cr, Mo, W; X = O, S, Se, Te) monolayers: A comparative study, Appl. Phys. Lett. **104**, 203110 (2014).

[73] T. C. T. Ting and T. Chen, Poisson's ratio for anisotropic elastic materials can have no bounds, Q. J. Mech. Appl. Math. **58**, 73 (2005).

[74] C. Huang, R. Li, and L. Chen, Anisotropic elasticity and abnormal Poisson's ratios in super-hard materials, AIP Adv. **4**, 127116 (2014).

[75] R. Li, Q. Shao, E. Gao, and Z. Liu, Elastic anisotropy measure for two-dimensional crystals, Extreme Mech. Lett. **34**, 100615 (2020).

[76] S. I. Ranganathan and M. Ostoja-Starzewski, Universal elastic anisotropy index, Phys. Rev. Lett. **101**, 055504 (2008).

[77] C. M. Kube and M. de Jong, Elastic constants of polycrystals with generally anisotropic crystals, J. Appl. Phys. **120**, 165105 (2016).

[78] J. Kang, H. Sahin, and F. M. Peeters, Mechanical properties of monolayer sulphides: A comparative study between MoS_2, HfS_2 and TiS_3, Phys. Chem. Chem. Phys. **17**, 27742 (2015).

[79] H. Lang, S. Zhang, and Z. Liu, Mobility anisotropy of two-dimensional semiconductors, Phys. Rev. B **94**, 235306 (2016).

[80] A. Rawat, N. Jena, D. Dimple, and A. De Sarkar, A comprehensive study on carrier mobility and artificial photosynthetic properties in group VI B transition metal dichalcogenide monolayers, J. Mater. Chem. A **6**, 8693 (2018).

[81] W. Li and J. Li, Ferroelasticity and domain physics in two-dimensional transition metal dichalcogenide monolayers, Nat. Commun. **7**, 10843 (2016).

[82] X. Xu, Y. Ma, T. Zhang, C. Lei, B. Huang, and Y. Dai, Prediction of two-dimensional antiferromagnetic ferroelasticity in an AgF_2 monolayer, Nanoscale Horiz. **5**, 1386 (2020).

[83] Z. Tu and M. Wu, Ultrahigh-strain ferroelasticity in two-dimensional honeycomb monolayers: From covalent to metallic bonding, Sci. Bull. (Beijing) **65**, 147 (2020).

[84] H. Fang, Y. Wang, S. Shang, and Z.-K. Liu, Nature of ferroelectric-paraelectric phase transition and origin of negative thermal expansion in $PbTiO_3$, Phys. Rev. B **91**, 024104 (2015).

[85] M. N. Blonsky, H. L. Zhuang, A. K. Singh, and R. G. Hennig, *ab initio* prediction of piezoelectricity in two-dimensional materials, ACS Nano **9**, 9885 (2015).

[86] H. Yin, J. Gao, G.-P. Zheng, Y. Wang, and Y. Ma, Giant piezoelectric effects in monolayer group-V binary compounds with honeycomb phases: A first-principles prediction, J. Phys. Chem. C **121**, 25576 (2017).

[87] W. Li and J. Li, Piezoelectricity in two-dimensional group-III monochalcogenides, Nano Res. **8**, 3796 (2015).

[88] P. Schwerdtfeger and J. K. Nagle, 2018 table of static dipole polarizabilities of the neutral elements in the periodic table, Mol. Phys. **117**, 1200 (2019).